Design of a Space-based Hyperspectral Characterization Sensor

Raymond H. Wright¹, Geoffrey Lake², Thomas Drouillard¹, Andrew I. Wernersbach¹, Kedar R. Naik¹, Michael Dittman¹, Matthew N. Tooth¹

¹BAE Space and Mission Systems ²Icebox Engineering

ABSTRACT

The ability to rapidly identify Resident Space Objects (RSOs) from intrinsic signatures is critical for complete Space Domain Awareness (SDA) and achieving space superiority. Hyperspectral Imaging (HSI) from visible to long-wave infrared can detect signature differences between RSOs that are created by material composition, manufacturing, and geometric differences. These differences are exploited using Machine Learning (ML) algorithms to enable single-observation identification of known objects and characterization of unknown objects. Space-based HSI systems provide access to critical wavelengths necessary for identification and characterization over ground-based HSI systems that are limited by atmospheric conditions, especially absorption features in frequencies where discriminating information lies.

In this paper, the advantages of HSI are discussed, including its ability to provide a more comprehensive view of space objects compared to traditional single-band or multispectral methods. The paper details the benefits of space-based HSI, including a quantification of the wavelengths that are important for identification and cannot be detected from ground-based systems. The paper explores the design and trade space of a space-based hyperspectral sensor, included parameters such as range, aperture, and spectral resolving power, and presents a 51-channel, ultra-wideband HSI system that can detect RSOs as small as 30cm, up to 10,000km range, and is composed of high Technical Readiness Level (TRL) components. The paper then details the modeling and simulation used to demonstrate the effectiveness of the sensor with ML algorithms in two experiments: identification of individual satellites of the same model, and characterization of an unknown satellite's material composition and mission.

The experimental results show that the HSI sensor and ML algorithms can accurately identify individual satellites within the same geometric design and different material compositions with greater than 89% accuracy for measured cases from a single HSI observation. The characterization experiment on realistic simulated data shows that the material composition of an unknown satellite geometry can be identified with greater than 74% accuracy. This study shows that a new capability to identify satellites and characterize their missions in a single observation could be achieved, and lead to greater space domain awareness.

1. INTRODUCTION

The Space environment is rapidly changing with record-breaking numbers of launches creating a new environment of peaceful and congested space. General Saltzman has stated "Space control is how the Space Force achieves space superiority" [1]. The ability to track is not sufficient, characterization is now required to identify benign from threatening, and where possible, to positively characterize satellites. Historically, this has been accomplished with kinematic correction, photometric correlation, and under special conditions, satellite to satellite imaging [2]. Hyperspectral imaging, commonly used for astronomy, and ML algorithms trained on HSI data has been shown to characterize and identify satellites [3] on their intrinsic material properties. To support the SDA mission, we proposed a space-based HSI system to eliminate the limitations of ground-based systems to improve space control. In this paper we demonstrate that a space-based hyperspectral instrument combined with machine-learning algorithms can be used in combination to support timely, broad area characterization and identification of the space domain which should be included in the SDA enterprise. This will be achieved by demonstrating possible space based HSI sensor design, measure its performance against realistic targets, and demonstrated the ability to leverage the signal detected up to 10,000km ranges to identify simulate satellites.

Spectral imaging is the term for collecting multiple individual wavebands by decomposing the received signal into its constituents. Color imaging is often performed using three wavebands on the Red, Green, and Blue (RGB)

wavelengths which yields much information for a human interpreter. Similarly, hyperspectral imaging collects many wavebands, between 10s anywhere to 1000s Additionally, HSI is often used to sample wavelengths beyond human vision and can capture discrete elements in any part of the electromagnetic spectrum. In Electro-Optical (EO) sensing, this spectrum includes visible, short, near, mid, and long-wave infrared (IR). Visible, short, and near-infrared make-up the reflected profile of a satellite (Fig 1). Mid and long wave are signals emitted by the satellites internal surface and temperatures. combination of the reflected and emitted profile creates a unique fingerprint that a ML algorithm can identify and classify. In this way, pairing HSI with ML can identify objects in a single observing period, modeled in this paper as under a minute, when compared to a library of unknown or expected signatures. Within Fig 1 are two spectra captured by a single observer.

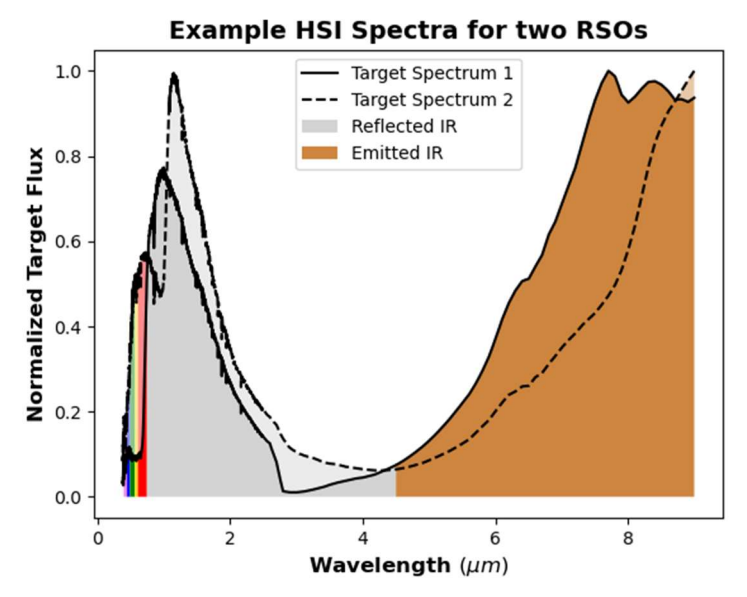


Fig 1: An example target spectrum with 1,677 color channels broken into visible, reflected, and emitted bandwidths.

The observer, for both observations, is located at the same range, elevation, azimuth, and solar phase angle. At this range, the target remains unresolved and appears as an indistinct point source on the detector. The modeled target exhibits the same spatial characteristics. The sole distinction between the two spectra lies in the material composition of the target. Despite the lack of spatial resolution, the spectral differences are evident and serve as a unique signature, enabling identification and characterization.

Ground-based hyperspectral imaging sensors such as OSIRIS [5] and PEPSI [6] are designed to perform astronomy missions. While they could be used to supplement SDA activities, they are limited by atmospheric conditions and location. Like all ground-based optical receiver systems, they can be inhibited by cloud cover and high particulate environments. They are also limited in sensitivity in the non-visible bands because of atmospheric absorption (Fig 2). HSI sensors like OSIRIS and PEPSI are design around these atmospheric absorption lines with OSIRIS capturing data in the visible and near-IR $(0.95-2.4\mu m)$ and PEPSI capturing data in the ultraviolet (UV), visible, and shortwave-IR spectrum $(0.38-0.91\mu m)$. These wavelengths center on the reflective side of the atmospheric window.

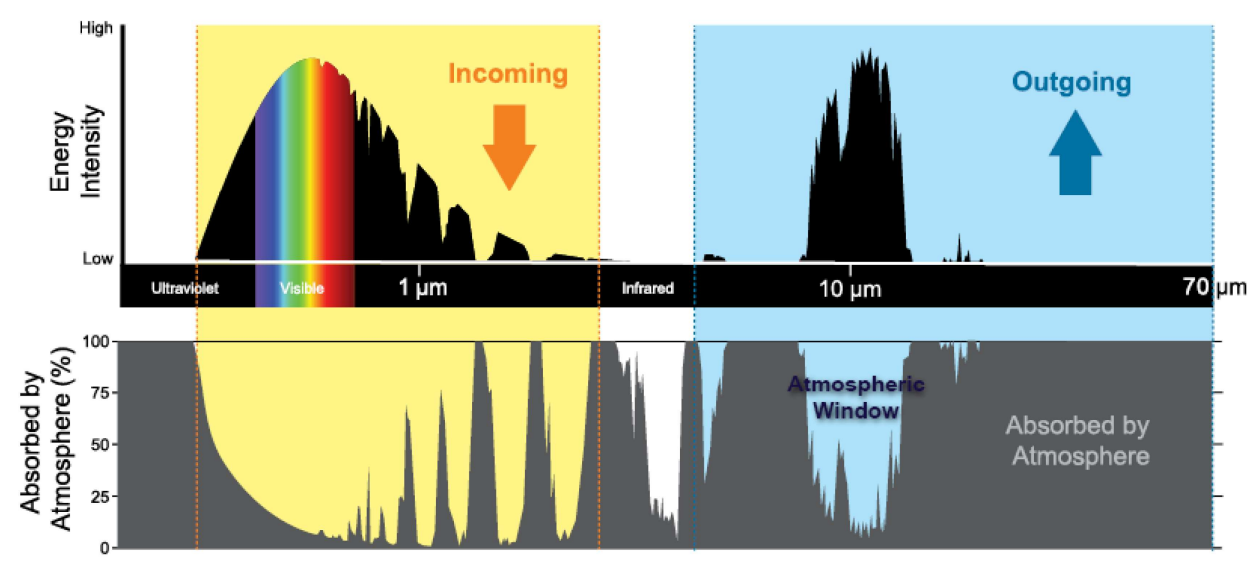


Fig 2: Earth's Atmospheric Window [7] relative to wavelength in micrometers. The atmospheric gaps (gray areas in the lower figure) are dominated by the absorptive qualities of water, oxygen, and carbon dioxide.

Within Fig 2, there are two figures. The top figure defines the areas of the spectrum that light can pass into or out of the earth. The rainbow and black curves show the detection windows for ground-based sensors. The bottom figure shows the inverse. The gray area is where incoming or outgoing light is absorbed by the atmosphere, creating detection gaps for a ground-based sensor.

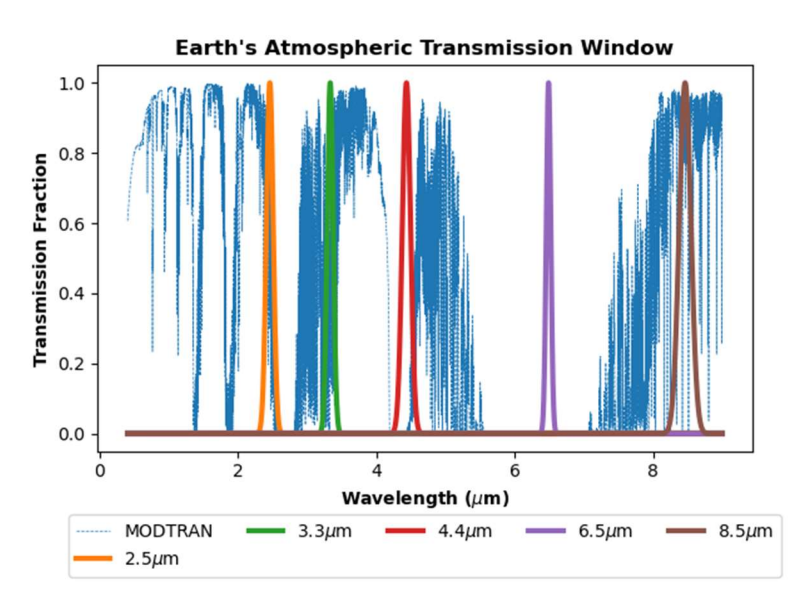


Fig 3: Earth's Atmospheric Transmission Window [8] (blue) and Naik's [3] optimal characterization wavelengths.

In 2024, [3] showed that five multispectral bands were needed to effectively distinguish between three RSO types, Active Satellite, Rocket Body, and Space Debris from a spacebased instrument. What is more important is that three of the five discriminating wavelengths (3.3µm, 4.4µm, 6.5µm) shown in Fig 3 have less than 50% average transmission through the atmosphere of the full width half max (FWHM), with 4.4μm, 6.5μm less than 2%. These results show valuable discriminating information is found in bands that cannot be observed from existing ground-based optical systems. These wavelengths are available from a space-based system that is not looking through an opaque atmosphere at those wavelengths.

In addition to the limitations of the atmosphere, ground-based HSI instruments are stationary and cannot provide the timely access due to geometric and lighting constraints. The PEPSI instrument is attached to the Large Binocular Telescope (LBT) Observatory located in Mt. Graham in Arizona. Timely tracking and dissemination of information of RSOs can only be achieved when the RSO is overhead. Space-based HSI systems can complete orbits in as little as 90 minutes enabling fast multi-object detection and characterization around the globe.

While space-based HSI data can be effective, the ability to field a space-based HSI sensor is also addressed. Prior space-based HSI sensors have ben used, they are primarily for Earth-viewing missions [9]. These sensors deployed in Low Earth Orbit (LEO) for viewing Earth are not optimized for SDA applications. In this paper, we provide a discussion (Section 2) on a notional sensor design and conclude with 51 spectral channels, 30cm aperture, designed to detect and characterize RSOs up to 10,000km range with high a TRL level. We also detail the development of high fidelity simulated data leveraging 3D models [10], applying materials to the surfaces and simulating the captured spectral content via FIST/COAST [24] at the HSI. In Section 3 we detail the ML algorithms and how we applied them to the simulated signatures. This is done with two experiments. Experiment 1 applies multiple material sets to the target models and classifies each model on the material composition. Experiment 2 trains on a subset of the models then attempts to classify the third unknown model. Section 4 presents the results of the ML classifiers and Section 5 concludes with a summary of the work and future path forward.

2. SENSOR DESIGN

According to NASA, "As of 2024, there are more than 45,000 human-made objects orbiting Earth, and these are just the ones we can track..." [11]. These satellites range from the small university CubeSats (small, standardized satellites defined by their cubic dimensions, with 10x10x10cm defined as 1U), to the International Space Station (ISS). With such a large variety of objects, the sensor mission design bounded the target sizes by commonality. Approximately 24% of the known objects are comprised of CubeSats and Starlink. According to Kulu [12], 2,714 CubeSats and Nanosatellites launched in 2024. As of August 2025, there have been 8,075 Starlink satellites that are currently in orbit and operational [13]. The approximate circular diameter of satellites within the CubeSat and Starlink categories exhibit a range of 0.25m to 25m. The space-based HSI sensor is designed around classifying unresolved targets to

limit the size of the telescope. A comprehensive trade study was conducted to assess various sensor design options under practical constraints:

Table 1: Evaluation criteria for a notional hyperspectral instrument design

ruote 1. Evaluation efficia for a notional hyperspectal instrument design		
Performance Considerations	Design Constraints / Considerations	
 Detect 30cm satellite at 10,000km or greater with SNR > 6 in the weakest channel Detect 10m satellite @ 10,000km or greater range with SNR > 10 in the weakest channel 	 Small apertures are lighter and reduce cost Reduce use of mechanisms for higher reliability and reduced cost Use High-TRL design and components 	
 Achieve a frame time < 5 seconds with SNR > 5 Expand detection capability into atmospheric gaps 	Optimize design for unresolved target detection	

The primary objective of this evaluation is to develop an operationally feasible system that balances technical capabilities with practical limitations.

2.1 Hyperspectral Performance Parameters

As stated earlier, a hyperspectral imager captures light from the scene and decomposes it into distinct color bands. Table 1 defines the evaluation criteria that this paper aims to satisfy. To start, the design trade balances three key factors: the number of spectral channels, the size of the sensor, and the system's sensitivity.

An important data point captured in Fig 3 is the spread of the optimal wavelengths needed for the characterization covers $2.5-8.5\mu m$. In [14], it is stressed that the SDA enterprise needs to expand the EO detection operations to include all visible through long-wave IR. The Near Infrared Spectrograph (NIRSpec) on the Webb telescope uses detectors that have high detection sensitivity over $0.6-5\mu m$ [15]. BAE has been working to expand this TRL 9 detector into an Ultra-Wideband sensor that maintains the high sensitivity and increases the detection range to $0.4-9\mu m$. In design trades for standard imaging system, total signal

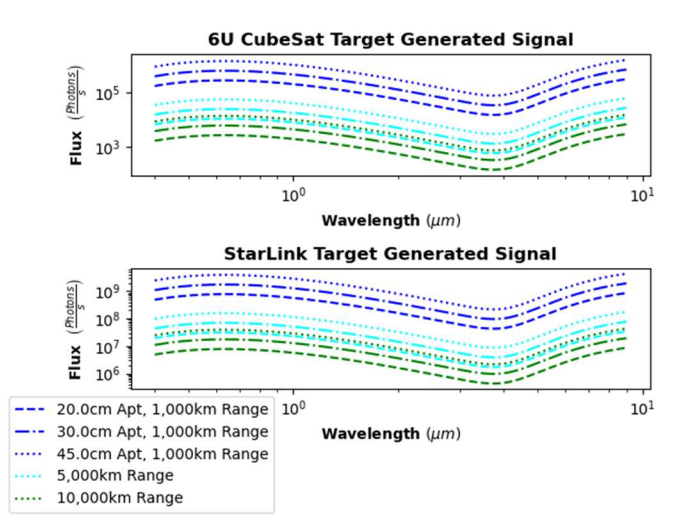


Fig 5: Starlink and a 6U CubeSat spectral fluxes for various aperture sizes and distances between the target and observer

captured is an important trade parameter, whereas an HSI the minimum signal needed for a color channel drives the design. Fig 5 shows the trade comparing target size, observer range from the target, and aperture size. All of the blue

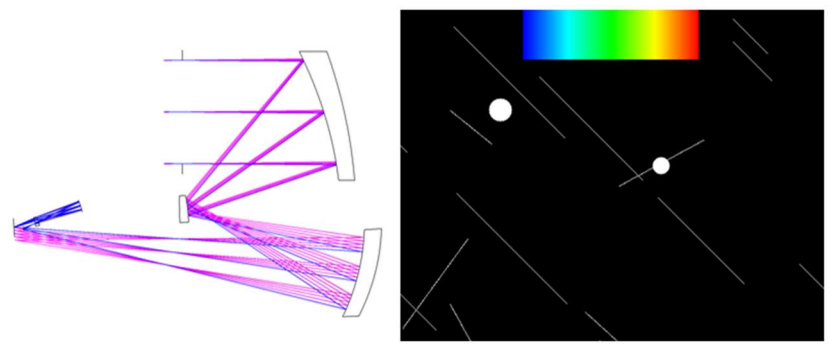
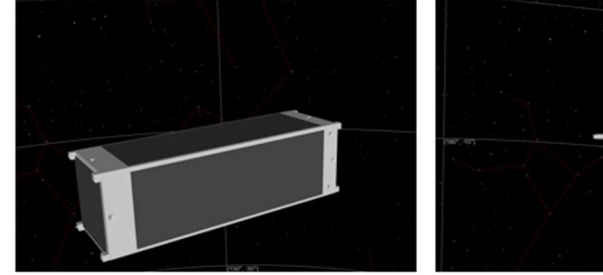


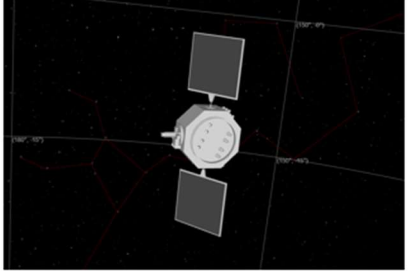
Fig 4: High TRL off-axis Three-Mirror Anastigmat (TMA) Imager and Hyperspectral instrument optical paths (Left). (Right) Close-up of the placement of the imaging path (dots and streaks) and spectral path (rainbow) on the detector.

lines represent a distance of 1,000 km between the observer and the target. The cyan and green lines are for 5,000km and 10,000km respectively. The line styles within the figures represent different aperture sizes. For all cases, the minimum captured signal occurs around 3µm which is close to one of the optimal bandwidths from [3]. Fig 4 contains the optical layout. A standard off-axis TMA design was selected to keep a compress the layout of the telescope. There are two optical paths that are imaged simultaneously by the detector. The image path is colored magenta and is used for target acquisition. The space vehicle will track the desired targets (dots in the image). Once tracked, the space vehicle will slew one of the dots into the pick-off mirror to place the target into the hyperspectral imaging path (blue lines). The 51 spectral channels are created when the target data is relayed through a Zinc Sulfide (TRL) prism. Then another set of images are captured in a small strip on the FPA which contains the hyperspectral content (see Fig 1) of the target. The integration times depend on the size of the target, but for the trade, it ranges from 0.08 - 2ms. Other design parameters for the HSI are a f-number of 6, field of view 1.2° , with a 30cm aperture and 250nm RMS wavefront error. Beyond the re-imaged pupil and including the FPA, the temperature needs to be maintained to 40K to control the dark current. The rest of the optical path is held at 55K to control the near field emissions. There are two types of cooling satellites, active and passive. Passive cooling requires large radiators and shields to keep the sensor in constant shade. Active cooling uses mechanisms and electronics. Active cooling units are much smaller than the large shades and radiators of passive cooling. The state-of-the-now solutions are called cryo-cooler. A cryo-cooler is a compact, closed-cycle, cooling systems that can maintain temperatures without the use of an expendable refrigerant. Two examples are BAE's TRL 9 Klondike [16] and Kodiak [17] cryo-coolers which have sufficient cooling power to cool an entire telescope to these temperatures while imparting very little jitter to a space vehicle.

2.2 Target Modeling and Data Generation

The evaluation of performance for the HSI sensor design is estimated using high-fidelity, simulated data, where materials with known and measured signals are overlayed onto 3-D models. The models are then articulated within the FIST/COAST [24] ray-tracing tool to generate unresolved signatures over differential geometries at mission relevant ranges. This method improves upon faster methods which use simple models such as spheres and cubes with mixed signals for data generation for unresolved imagery but lack the real impacts of spacecraft complexity and viewing that is necessary to fingerprint one satellite from another. Every RSO in orbit will have a distinct fingerprint that is deterministic from its geometry and material makeup. All spectral content for an unresolved target is contained within a single pixel. With the inclusion of geometry, the reflection and the emission profile generate a unique fingerprint that is identifiable.





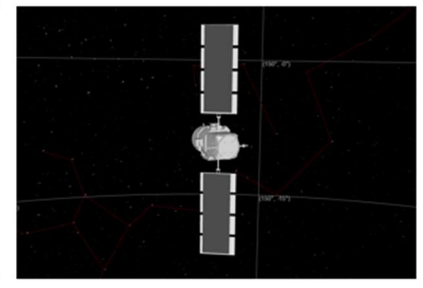


Fig 6: (Left) 1U x 3U CubeSat. (Middle) NASA DSCOVR. (Right) NASA CALIPSO

Three, highly detailed models selected from NASA's model database [10] are shown in Fig 6 and detailed in Table 2 which covers a range of target sizes.

Table 2: Target definition with bounding dimensions

Small Sized Target	Medium Sized Target	Large Sized Target
CubeSat	DSCOVR	CALIPSO
0.1m x 0.1m x 0.34m	3.1m x 1.1m x 1.2m	9.5m x 2.4m x 1.9m

While the models are geometrically accurate, they contained no material information. Materials were added to each model based on spectra collected and stored in BAEs database. The materials selected are primary materials used on spacecraft exteriors, such as solar panels, thermal and structural components, and paints which would be the largest contributors of spectra an HSI sensor would observe.

Table 3: Materials applied to the Target Models

1 4010 51 111	racie 5. Materials applied to the rarget Medels		
Category	Material ID	Material Name	
Metal	1	Aluminum Alloy	
Metal	2	Titanium	
Metal	3	Magnesium Alloy	

Category	Material ID	Material Name
Paint/MLI	4	White Paint
Paint/MLI	5	MLI
Paint/MLI	6	Aluminized Mylar
Glass	7	Fused Silica
Glass	8	Solar Cell
Glass	9	Silicon, Solar Cell

The materials selected in Table 3 are common and found on many spacecrafts' external surfaces. For each model in Fig 6, the black panels had a glass material applied for the solar cells. The gray portion of the model used a metal, and on one surface of the body was covered by a Paint/MLI material. A total of 18 unique model and material combinations were generated to create the simulated data, as shown in Table 4.

Table 4: Target Model and Material Combinations

Table 4: Target Model and Material Combinations			
Target	SV	Solar Panel	Single Surface
Model	Material ID	Material ID	Material ID
CubeSat A	1	4	7
CubeSat B	2	5	8
CubeSat C	3	6	9
CubeSat D	1	5	9
CubeSat E	2	6	7
CubeSat F	3	4	8
DSCOVR A	1	4	7
DSCOVR B	2	5	8
DSCOVR C	3	6	9
DSCOVR D	1	5	9
DSCOVR E	2	6	7
DSCOVR F	3	4	8
CALIPSO A	1	4	7
CALIPSO B	2	5	8
CALIPSO C	3	6	9
CALIPSO D	1	5	9
CALIPSO E	2	6	7
CALIPSO F	3	4	8

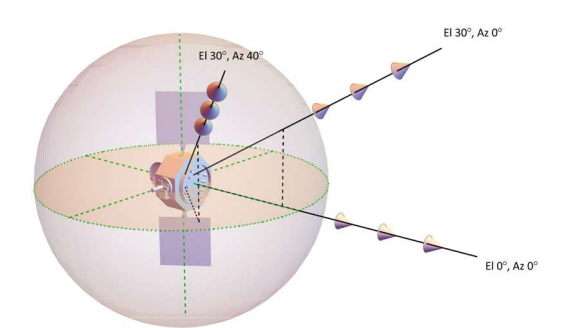


Fig 7: Sensors positioned at three target ranges along each of three lines of sight. The DSCOVR model (centered at the origin, oriented consistently with the COAST simulations, but not shown here to scale), provides a reference to the sensor viewing angles.

Capturing the effects of the geometric interactions between the Sun, target model, and observer required generating 9 HSI models placed at different azimuth, elevation, and ranges. Varying the elevation, azimuth, and range accounts for the glint and other non-Lambertian reflections, see Fig 7. The two elevation angles used are 0° and 30° . The two azimuth angles are 0° and 40° . The observing HSI sensor were placed at 6,000km, 8,000km and 10,000km. For each sensor location, the Solar Phase Angle (SPA) was shifted 180 times to capture the effects of incident energy on the targets. Since the HSI is using an Ultra-Wideband detector $(0.4 - 9\mu\text{m})$, changing the solar phase angle impacts the reflection and emission profiles of the targets. At some phases, the target spectrum will be dominated by the visible spectrum, and when the target is in shadow, it will be dominated by its thermal emissions.

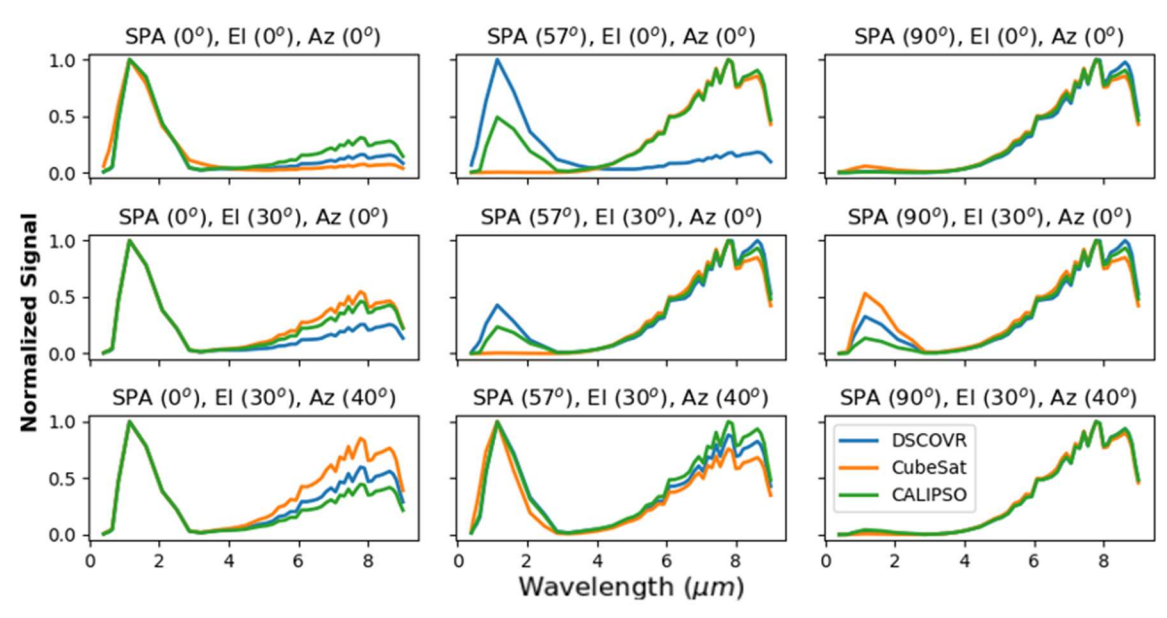


Fig 8: Example spectrum for CubeSat A, DSCOVR A, and CALIPSO A at different SPAs, elevations, and azimuths. The observing HSI is located 10,000km from the target models.

DSCOVR, CubeSat, and CALIPSO are represented by the blue, orange, and green colored lines. The left column of figures contains spectra for each target with a SPA of 0° . The middle column shows the spectral captured with an SPA of 57° . The right column of data happens with an SPA at 90° . From top to bottom, in the row direction, the elevation and azimuth change. Changes in the SPA greatly impact the visible and infrared lobes. Different elevations and azimuths capture different phases (geometry) of the target models. At a SPA of 57° and looking from top to bottom, the reflected portion of the spectrum ($< 4\mu m$) significantly changes. This is due to the non-Lambertian reflection (glints) of that portion of the spectrum dominating (or not).

The FIST/COAST [24] generated data contains 1,677 color channels per captured spectrum. To match the expected output of the HSI sensor, the 1,677 color channels are converted to 51 color channels using the Signal Response Function (SRF) of the as-designed HSI.

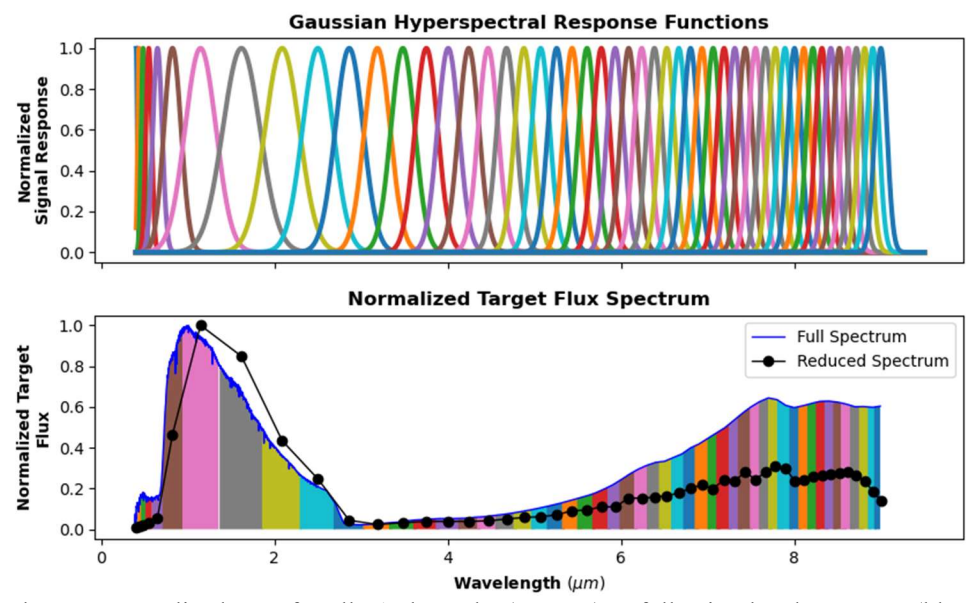


Fig 9: (Top) The HSI normalized SRF for all 51 channels. (Bottom) A fully simulated spectrum (blue line) and the reduced spectrum with each of the 51 channels coverage

In total, over 29,000 spectra were generated for the training, validation, and verification data sets. Every spectrum had 1,677 channels of color defined (blue line in Fig 9). Each data set was reduced using the SRF down to 51 channels of color (black line example in Fig 9, with the center wavelength marked with dots) to match the HSI design. The shade regions shows the portion of the spectra that was reduced to the small channel. NOTE: the color of the shaded region matches the color directly above it on the top plot.

3. CHARACTERIZATION AND IDENTIFICATION

The ability to identify individual satellites by characteristics other than their kinematic state in short timelines is necessary to reduce cross-tagging of SDA observation. We define *identification* in this research as the ability to tell distinct copies of the same satellite configuration, i.e. we can differentiate between two cubesats based only on the spectral signatures. This identification is analogous to identifying a single "tail number" from constellation of same satellites, such as Starlink, or Thousand Sails.

We define *characterization* in this research as the ability to infer information about any satellite, based on the signature. An example of this would be that certain material combinations (and their spectral signatures) and ratios would be indicative of radio-frequency sounders, while other material compositions would be indicative of EO systems. This ability to infer mission, based on material compositions can be valuable especially in new launches where the intent and capability of a new space vehicle are unknown and not easily imaged.

The exploitation of hyperspectral imagery using ML-based approaches has been explored over the past decade, in applications such as agricultural entity characterization [18][19][20] and has more recently been expanded to space-object-identification efforts [3][21]. Many of these works have specifically made use of decision-tree-based approaches to performing classification, which Xu et al. attributes to the complexity of deep neural networks which comes from having larger parameter sizes, which require more powerful hardware to utilize effectively. As such, the present work uses gradient boosting – a decision-tree-based approach – approach to characterize space-object material compositions.

The present study focuses on two experiments: an identification experiment, and characterization experiment. The first experiment assesses the ability of the ML-based approach to identify the "tail numbers" of each target. In Table 3, the six tail numbers correspond to the material composition of the target model, cases A - F. The second experiment expands this capability into the characterization of an unknown satellite. In this experiment, the classifiers are trained on two of the target models and all material cases, CubeSat A - F and CALIPSO A - F. Then unknown targets corresponding to DSCOVR cases A - F are characterized by the ML classifiers.

By performing these two experiments on the synthetic hyperspectral dataset, the authors will establish a) ML-based approaches perform very well in identifying the tail number of a known target model, and b) ML-based approaches demonstrate promising performance in characterizing an unknown target model by identifying the material composition of that satellite as compared to existing material signature models.

3.1 Data Partitioning

In performing the tail number identification and material characterization experiments, the data generated must be split into a training, validation, and test set as in Fig 10. For each experiment, the training set represents the "known" set of samples from which the classifiers will learn defining characteristics. The validation set represents data from this distribution which has not been explicitly handed to the classifier to learn from and is used to tune hyperparameters (section 3.3). The test set represents the set of samples containing similar features to the trained data from a potentially different distribution. As the experiments vary on what they consider to be known and unknown, each requires its own variation of the data partitioning.

For the first experiment, by assuming every target model and all its tail numbers (A - F) are known, a standard stratified data split can be performed on the whole dataset. This means 70% of the data will belong to the training set, 10% of the data will belong to the validation set, and 20% of the data will belong to the test set, where stratification ensures each set has an equal number of each distinct satellite model within it.

For the second experiment, assuming only CubeSat A – F and CALIPSO A – F are known, then the training and validation sets should come from a distribution of these samples. Exactly 2/3 of our dataset belong to these two cases. As such, the training and validation set come from an 87.5% / 12.5% split of these samples. The test set consists solely of 1/3 of samples belonging to DSCOVR A – F. This is analogous to having data on multiple satellite configurations with material compositions (as may be found by various mission packages on similar buses). The test data is then analogous to having seen a new satellite configuration with similar material composition, which could imply the same mission package as other satellite configurations.

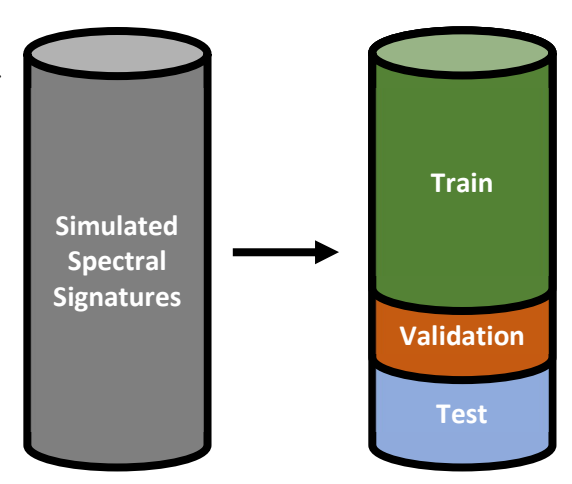


Fig 10: Partitioned data buckets representing the format of the data partitions for the tail number identification and material characterization experiments.

3.2 Data Processing

For both experiments, the models were trained on the 51-channel no-noise pristine data (Fig 9). To mitigate the impact of relative intensity between target models of different sizes, the values across the 51 color channels of each individual spectrum in the data have been min-max normalized. This is performed to demonstrate that the algorithms are using material signatures to discriminate, not the relative intensity or brightness which can be done with broad-band EO systems. Within each experiment, there will be a test set of the same samples, one which is pristine (no noise added), and one which contains noise. Pristine data is used as a control, and the noisy data is modeled to include some expected effects of a real sensor. The noise added to this set consists of Gaussian white noise, representing detector read noise, and Poisson noise, representing scene shot noise, and were incorporated into each of the 51 color channels for data within the respective test set for each experiment. A visualization of each of these test buckets can be found in Fig 11.

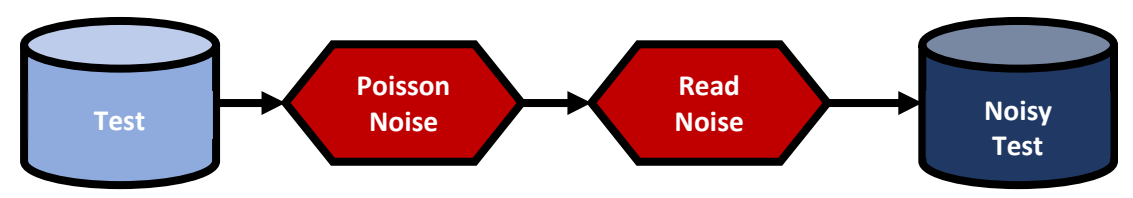


Fig 11: Test-set noising process

3.3 Machine Learning Framework

The ML-based approach described in the present work consists of a series of individual binary classifiers for each of material configurations A – F. Each of these binary classifiers is an instance of an XGBoost [22] module, which is a specific implementation of a gradient-boosted decision tree. Each of these binary classifiers are trained to minimize the binary-cross-entropy loss function. For each classifier, a Bayesian optimization routine, implemented with Optuna [23], is wrapped around the training process to optimize the hyperparameters of the classifier to produce the greatest performance. After the optimal set of binary classifiers is produced, testing is performed by running each test-set sample through each of the binary classifiers to collect a probability score, after which the highest probability of the six is selected to represent the predicted class. This set of predicted classes is used to compute several metrics, with the primary metric considered in this study being the true positive rate (recall) between the predicted and actual classes. Recall is a proportion of correct predict of a class to the actual number of instances for a given class, which measures how many samples belonging to that class have been correctly classified. A visualization of the machine-learning pipeline described here can be found in Fig 12.

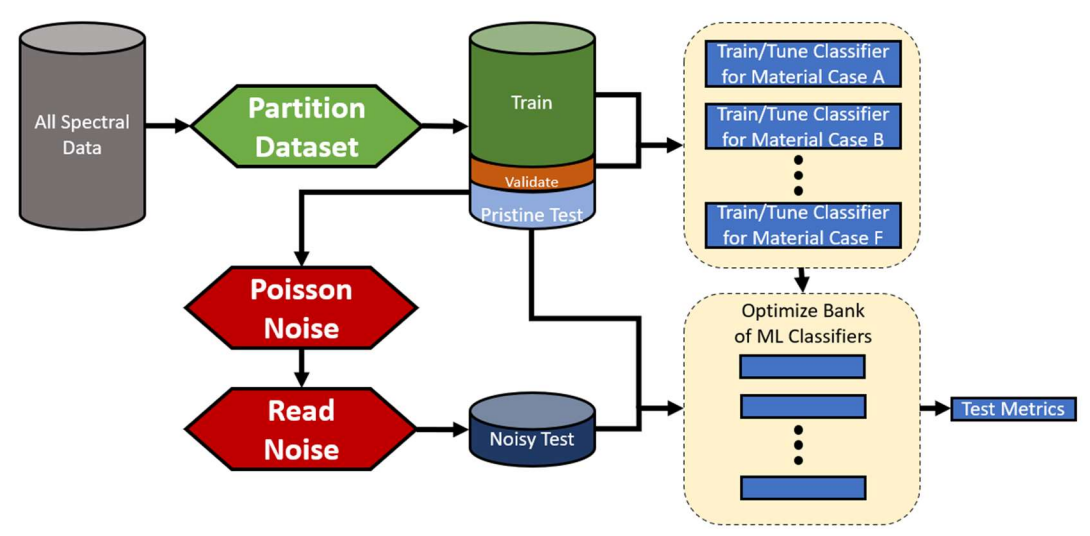


Fig 12: Pipeline describing the process to handle the data and use it to perform identification and characterization experiments.

4. RESULTS

Having established a pipeline by which the data could be processed and digested by ML-based classifiers, experiments were performed to (a) identify specific versions ("the tail number") of a known satellite model, and (b) characterize an unknown satellite by identifying a material composition like known satellites. During testing, a sample consists of the normalized intensity across the 51 channels and associated meta-data. This is analogous to a single less than 1 second observation from the HSI sensor.

4.1 Known Target Model Tail-Number Identification

The experiment to identify a known target model can be broken up into the three individual target models for which this test was performed: CubeSat, DSCOVR, and CALIPSO. Each of the classifiers for cases A – F have been trained on 70% of the pristine samples, tuned using 10%, and tested on the final 20%. The final 20% has two variants for which testing was performed, the pristine version and the noised version. As these spectra are passed through the six binary classifiers, the one with the highest probability score is taken to be the prediction for that spectrum This prediction is then run against the true prediction for every sample in the test set, from which a confusion matrix can be built to represent the ratio of correct predictions to mistakes, broken down by individual satellite configurations. This can be seen in Fig 13, where the left column demonstrates that predicting the tail number of a known satellite body without noise is done correctly for all test samples. When realistic impacts of shot and read noise are included, performance degrades as expected. Excitingly, the largest degradation impact of noise (CubeSat–A) detects more than 75% of samples belonging to that configuration using a space-based 51 channel HSI system where each sample comes from a less than 1 second observation. Apart from CubeSat-C and CubeSat-D, greater than 92% of all samples are correctly identified for all other cases. In fact, the average true positive rate for all CubeSat cases was 89%, for all DSCOVR cases was 96% and for all CALIPSO cases was 99%.

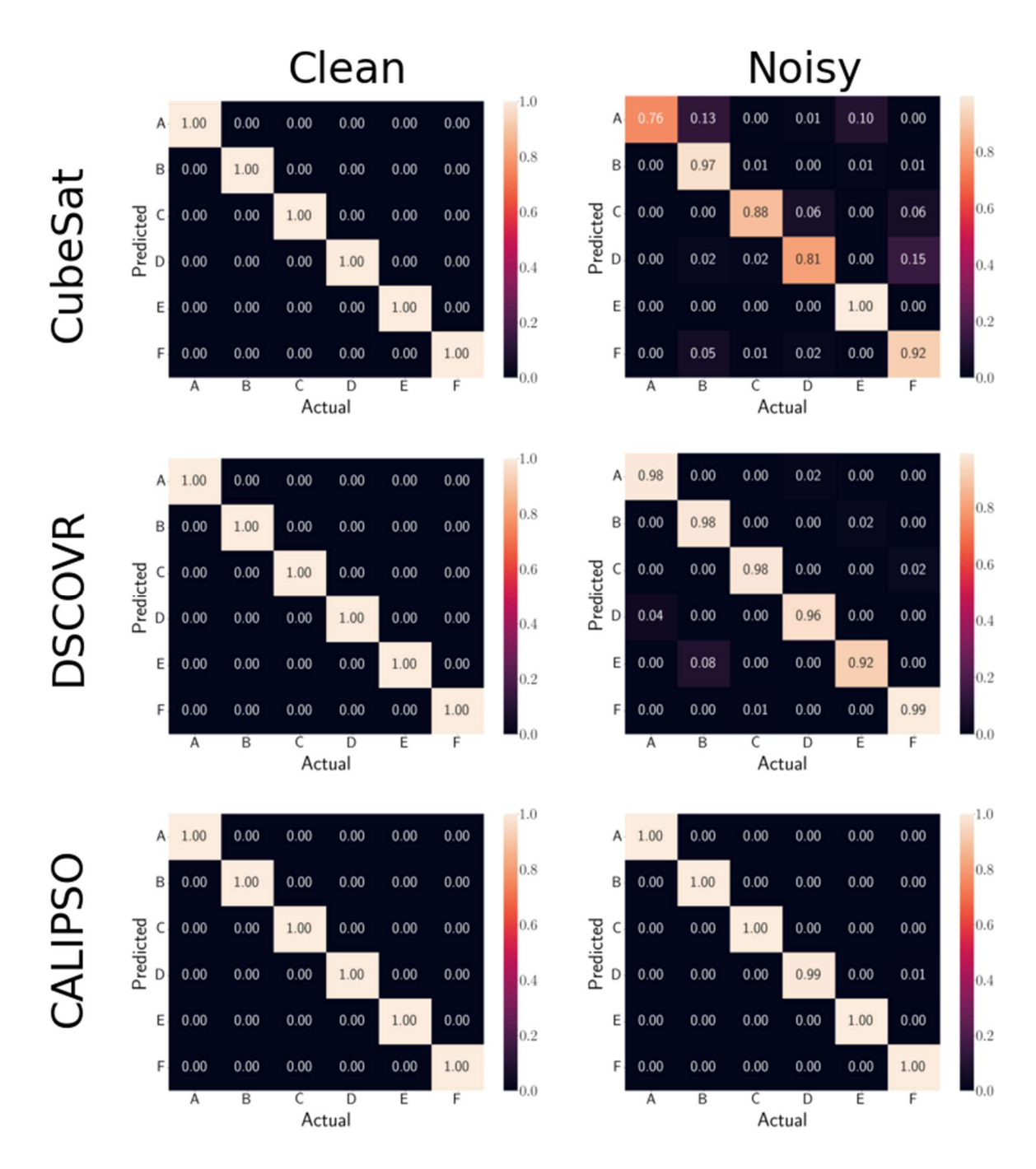


Fig 13: Confusion matrix of tail number predictions on known satellite models for both pristine test set (left column) and noisy test set (right column)

4.2 Unknown Target Model Material Characterization

The experiment to characterize the material composition of an unknown target model can be broken up into the two individual target models which the classifiers will be trained on, CubeSat and CALIPSO, and the one individual target model which the performance will be evaluated, DSCOVR. Each of the classifiers for material compositions A – F have been trained on 87.5% of the pristine samples in CubeSat and CALIPSO, tuned using the other 12.5%, and tested on the entirety of the DSCOVR data. The DSCOVR test was also performed on the pristine version and the noised version of the data. The testing process is shared with that of the previous experiment, where the series of binary classifiers is iterated to aggregate probabilities, for which the maximum is selected. The confusion matrix

demonstrating these results can be seen in Fig 14. The left matrix demonstrates the prediction of the tail number of an unknown satellite model without noise. In the worst case (DSCOVR-A), the classifier can correctly characterize 61% of the total instances of that case, but in the best case (DSCOVR-E), that goes up to 100%. In most cases, the inclusion of noise does not degrade performance by much. The most noteworthy drop appears in the classification of Material Case D, where the model is 11% less likely to characterize this material case in the presence of noise. Across all cases, the true positive rate does not change much with the inclusion of noise, with merely a drop from 75% to 74%.

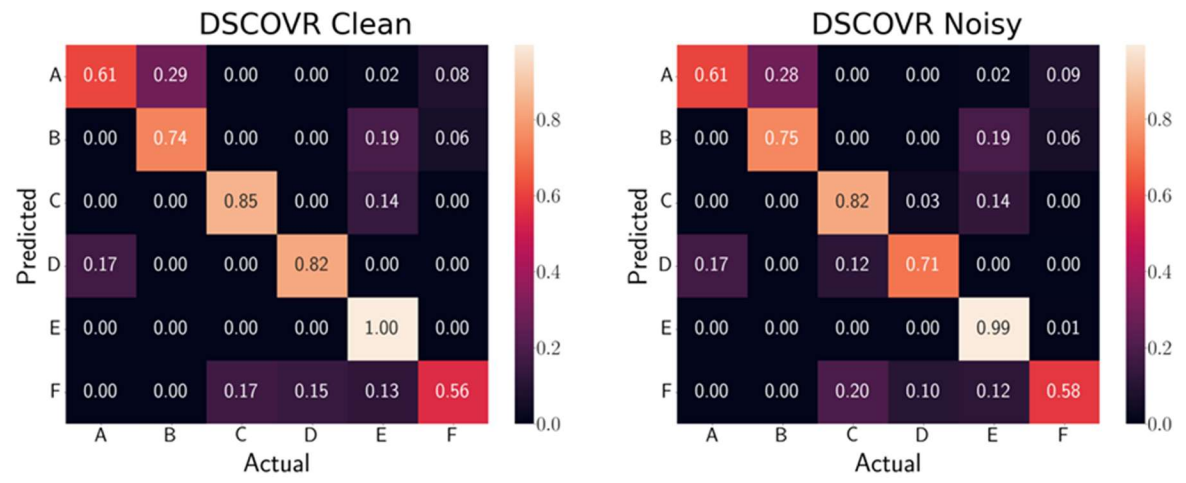


Fig 14: Confusion matrix of tail number predictions for the unknown satellite body for both the pristine test set (left matrix) and noisy test set (right matrix)

4.3 Important Wavelengths

During training of the classifiers used in these experiments, the architecture was designed to record properties of the decisions used in the gradient-boosted decision trees. That is, when a split was made between measured values at the distinct wavelengths, the amount of information gained, typically measured by number of samples separated between different categories was measured, and used to rank how important that wavelength is. Using this process, it was possible to extract the importance of each wavelength as it pertains to making classification decisions. Since the system in place aggregates decisions from six different classifiers, the wavelength importances were summed to determine the overall importance of each band to the system.

By analyzing how important each wavelength is, it was possible to compare how feasible it is to perform these experiments using a ground-based system in place of a space-based one. This is done by comparing the significant bands collected from each experiment against atmospheric absorption windows. For this analysis, the highest bands responsible for 99% of classification decisions were compared against the corresponding ground-based bands with at least 50% transmissivity through the atmosphere.

For the case of the known satellite body tail-number identification experiment, Fig 15 shows the importance of every wavelength broken down by satellite model type, with a background curve representing the atmospheric transmission window. For the CubeSat tail-number classifiers, the number of bands required to make 99% of the classifications is 43. 37% of these bands fall in ranges with less than 50% atmospheric transmission. For the DSCOVR tail-number classifiers, the number of bands required to make 99% of the classifications is 41. 32% of these bands fall in ranges with less than 50% atmospheric transmission. For the CALIPSO tail-number classifiers, the number of bands required to make 99% of the classifications is 43. 35% of these bands fall in ranges with less than 50% atmospheric transmission.

For the case of the unknown satellite body material characterization experiment, Fig 16 shows the importance of every wavelength broken down by satellite model type, with a background curve representing the atmospheric transmission window. The number of bands required to make 99% of the classifications is 43. 40% of these bands fall in ranges with less than 50% atmospheric transmission.

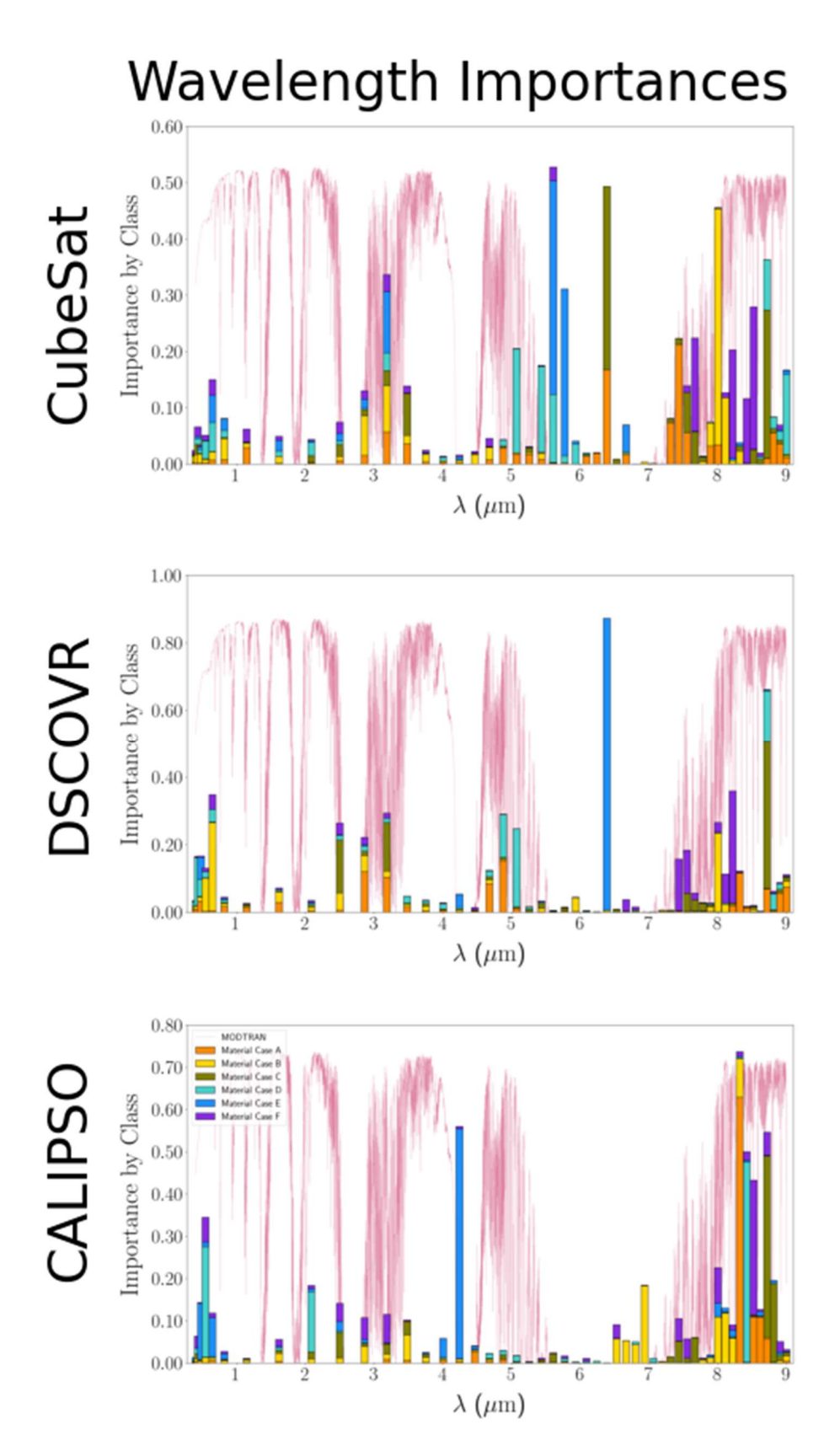


Fig 15: Feature importance plots overlayed with the atmospheric windows for Experiment 1

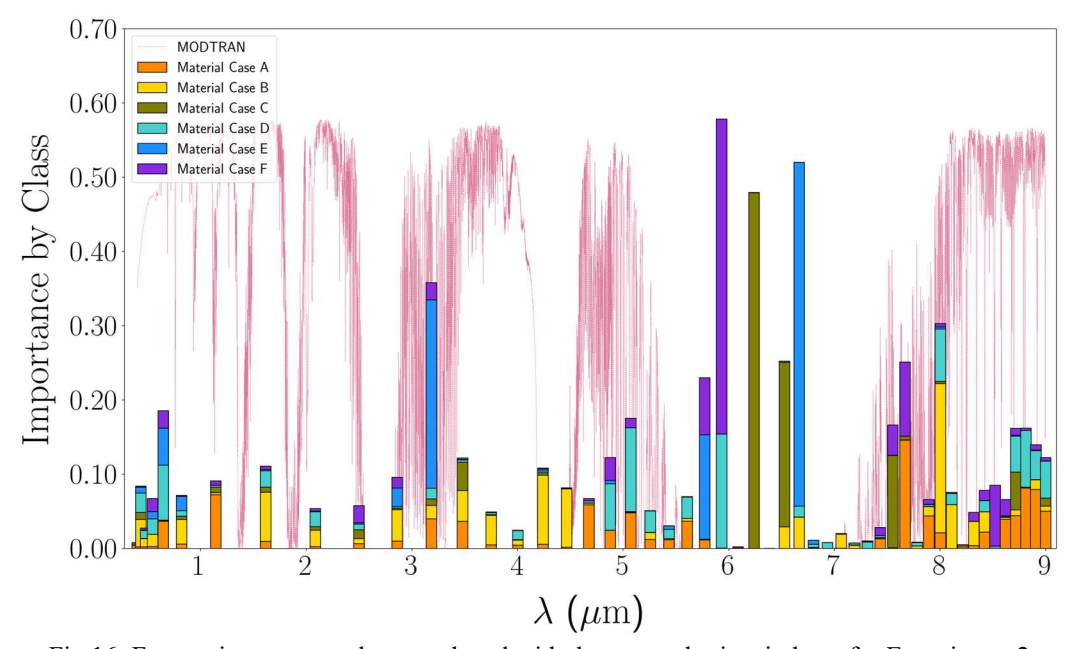


Fig 16: Feature importance plots overlayed with the atmospheric windows for Experiment 2

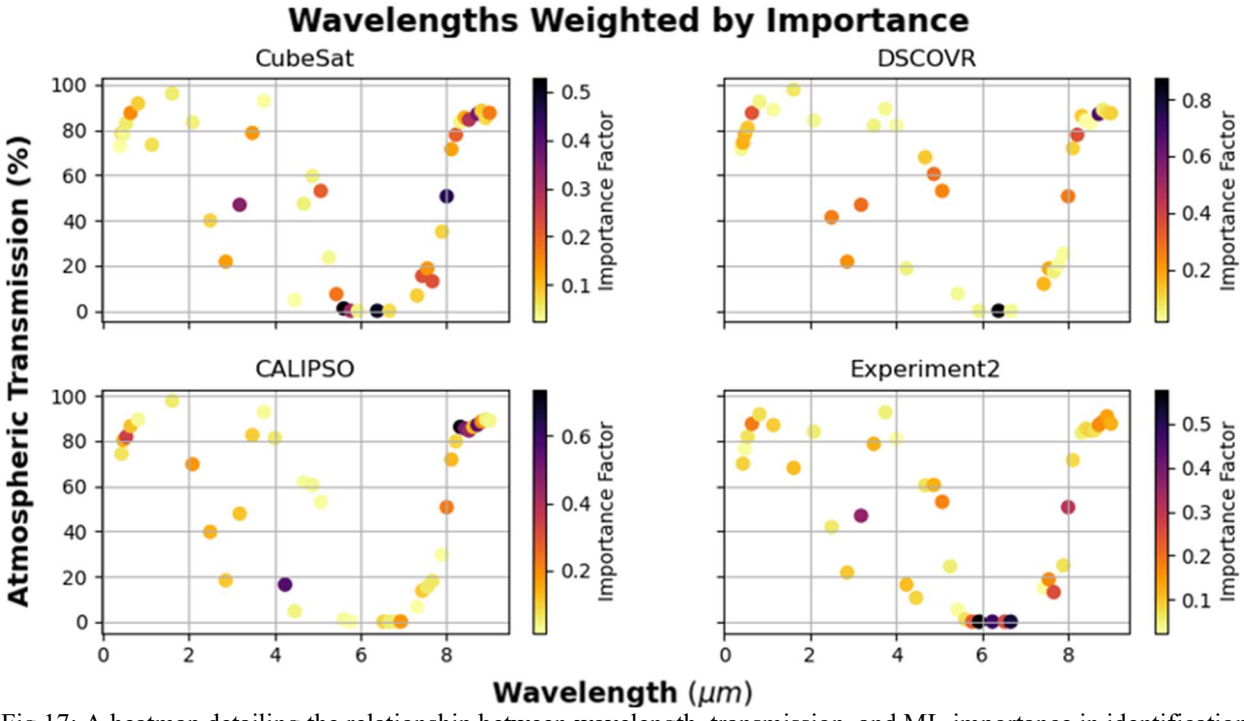


Fig 17: A heatmap detailing the relationship between wavelength, transmission, and ML-importance in identification and characterization.

Fig 17 is an alternative way to view Fig 15 and Fig 16. Along the x-axis defines the center wavelengths of the HSI. The y-axis represents the average atmospheric transmission over the channel bandwidth (defined in Fig 9). The color bar or heatmap characterizes the importance of that band to the ML-algorithm. Lighter colors are of lower importance, and darker colors denote higher importance. For CubeSat, DSCOVR, and Experiment 2 (characterizing the unknown target), many of the higher important wavelengths have an atmospheric transmission below 30%. Only CALIPSO has most of their important wavelengths in an atmospheric window. However, in ALL cases, the visible through shortwave IR spectrums were of medium to lower importance.

5. CONCLUSION

The integration of space-based Hyperspectral Imaging (HSI) systems with Machine Learning (ML) algorithms presents a promising solution for enhancing Space Domain Awareness (SDA) and achieving space superiority. By leveraging the unique spectral signatures of satellites, a space-based HSI system can provide timely and broad area characterization and identification of objects in space. This paper has presented a design of a HSI sensor and ML algorithm suite which creates a system that (a) can detect unresolved satellites ranging from 30cm to 13m at 10,000km range from the observer and (b) identify or characterize a satellite from its material properties. This design shows that space-based HSI systems are not a "far in the future" capability but could be fielded in the near-future given the high TRL nature of the majority of the system components.

This system has shown that satellites of the same geometry can be individually identified within a single HSI observation. This can be used to discriminate between two similar satellites, where one may be benign and the other may have ill-intent, based on the material differences of those satellites' payloads, where the different materials generate a unique signature that can be used to assign an individual "tail number" to that satellite. The system as modeled can identify the individual satellite with an average rate **greater than 89%** for the CubeSat and **greater than 96%** for DSCOVR and CALIPSO tail numbers.

When the system is challenged to characterize a new satellite configuration (3-m RSO that was not in any training data), the system can identify the material composition an average success rate greater than 74%. This would enable an observer to determine the material composition of this new satellite and estimate its mission and capabilities from a single observation. This is possible because certain materials and ratios are indicative of missions, such as the materials of RF-sounding apertures.

The study has shown that for accurate characterization and identification of geometrically accurate targets, many of the important wavelengths reside within the atmospheric gaps that block a ground-based HSI sensor from detecting. Further analysis of the results has shown that many of these wavelengths, reside in areas of the atmospheric windows with a transmission less than or equal to 50%.

The limitations of ground-based HSI systems such as atmospheric interference and restricted spectral ranges, can be overcome with a space-based system. By collecting data across multiple wavebands, including visible, near-infrared and long wave infrared, a space-based HSI system can create a comprehensive and accurate picture of the space environment.

The proposed system, combining HSI and ML algorithms has the potential for:

- 1. Timely and accurate characterization and identification of objects based on their intrinsic material properties.
- 2. Providing real-time updates on the space domain, enabling more effective space control.
- 3. Enhancing SDA capabilities, supporting the Space Force's mission to achieve space superiority.

By advancing the capabilities of space-based HSI systems and ML algorithms, we can improve our understand of the space environment and enhance our ability to control and protect our space assets.

6. ABBREVIATIONS AND ACRONYMS

Acronym	Description
ЕО	Electro-Optical
FWHM	Full Width Half Max
HSI	Hyperspectral Imager
IR	Infrared
ISS	International Space Station
LBT	Large Binocular Telescope
LEO	Low Earth Orbit
ML	Machine Learning
NIRSpec	Near Infrared Spectrograph
RBG	Red - Green - Blue
RSO	Resident Space Objects

Acronym	Description
SDA	Space Domain Awareness
SPA	Solar Phase Angle
SRF	Signal Response Function
SWAP	Size Weight and Power
TMA	Three-Mirror Anastigmat
TRL	Technology Readiness Level
UV	Ultra-Violet

7. REFERENCES

- [1] Erwin, S, "Space Force chief calls for greater focus on 'space superiority", Space Force chief calls for greater focus on 'space superiority' SpaceNews (2025)
- [2] B. M. Kennedy, P. Doran, R. S. Hughes, K. Hughes, R. Bocchino, D. Lubey, D. Mages, L.Fesq "Satellite-to-satellite imaging in support of LEO optical navigation, using the ASTERIA CubeSat", Proc. SPIE 11505, CubeSats and SmallSats for Remote Sensing IV, 115050H (22 August 2020), https://doi.org/10.1117/12.2567794
- [3] Naik, K., Wernersbach, A., Robinson, A., Nilson, M., Wiemokly, G., Tooth, M., Wright, R., "ML-Driven Optimal Design of Multispectral Instruments for the Characterization of Resident Space Objects" in [Proceedings of the Advanced Maui Optical and Space Surveillance (AMOS) Technologies Conference] (2024)
- [4] Jakobsen, P., Ferruit, P., Alves de Oliveira, C., Arribas, S., Bagnasco, G., Barho, R., ... Zincke, C. (2022). The Near-Infrared Spectrograph (NIRSpec) on the James Webb Space Telescope I. Overview of the instrument and its capabilities. Astronomy & Astrophysics, 661, A80. https://doi.org/10.1051/0004-6361/202142663
- [5] The Ohio State University, "Ohio State Infrared Imager/Spectrometer (OSIRIS) Ohio State InfraRed Imager/Spectrometer (OSIRIS) | Department of Astronomy, (2025)
- [6] Large Binocular Telescope Observatory, "PEPSI", PEPSI: Science Ops Large Binocular Telescope Observatory (LBTO), (2025)
- [7] National Oceanic and Atmospheric Administration. The Atmospheric Window. 10 Apr. 2023, https://www.noaa.gov/jetstream/satellites/absorb
- [8] A. Berk, P. Conforti, R. Kennett, T. Perkins, F. Hawes, and J. van den Bosch, "MODTRAN6: a major upgrade of the MODTRAN radiative transfer code," Proc. SPIE 9088, Algorithms and Technologies for Multispectral, Hyperspectral, and Ultraspectral Imagery XX, 90880H (June 13, 2014); doi:10.1117/12.2050433
- [9] Transon, J.; d'Andrimont, R.; Maugnard, A.; Defourny, P. Survey of Hyperspectral Earth Observation Applications from Space in the Sentinel-2 Context Remote Sensing, vol. 10, 2018.
- [10] NASA. 3D Resources. NASA Science, https://science.nasa.gov/3d-resources/. Accessed 2 Aug. 2025.
- [11] "Make Way for Satellites", NASA Spinoff, National Aeronautics and Space Administration, 11/02/2025, Make Way for Satellites | NASA Spinoff
- [12] Kulu, E., "CubeSats & Nanosatellites 2024 Statistics, Forecast and Reliability", International Astronautical Congress (IAC 2024), October 2024, IAC-24.B4.6A.13
- [13] McDowell, J. (2025, August 1). Starlink satellite statistics. Jonathan's Space Report. Retrieved from https://planet4589.org/space/stats/star/starstats.html
- [14] Wright, R., Gordon, M., Van Cleve, J., Schroots, H., "Infrared Sensing for Space-Based Space Domain Awareness" in [Proceedings of the Advanced Maui Optical and Space Surveillance (AMOS) Technologies Conference] (2023)
- [15] Jakobsen, P., Ferruit, P., Alves de Oliveira, C., Arribas, S., Bagnasco, G., Barho, R., ... Zincke, C. (2022). The Near-Infrared Spectrograph (NIRSpec) on the James Webb Space Telescope I. Overview of the instrument and its capabilities. Astronomy & Astrophysics, 661, A80. https://doi.org/10.1051/0004-6361/202142663
- [16] Taylor, R., et al., "Ball Klondike Cryocooler System Design, Development, Qualification and Performance," Cryocoolers 22, ICC Press, Boulder, Colorado (2018), pp. 53-62
- [17] Taylor, R., et al., "BAE Kodiak Cryocooler System Design, Development, Qualification and Performance," Cryocoolers 23, ICC Press, Boulder, Colorado (2023), pp. 81-88
- [18] Ballanti, L.; Blesius, L.; Hines, E.; Kruse, B. Tree Species Classification Using Hyperspectral Imagery: A Comparison of Two Classifiers. Remote Sens. 2016, 8, 445. https://doi.org/10.3390/rs806044
- [19] Xu, S.; Liu, S.; Wang, H.; Chen, W.; Zhang, F.; Xiao, Z. A Hyperspectral Image Classification Approach Based on Feature Fusion and Multi-Layered Gradient Boosting Decision Trees. Entropy 2021, 23, 20. https://doi.org/10.3390/e23010020

- [20] A. I. Champa, M. F. Rabbi, S. M. Mahedy Hasan, A. Zaman and M. H. Kabir, "Tree-Based Classifier for Hyperspectral Image Classification via Hybrid Technique of Feature Reduction," 2021 International Conference on Information and Communication Technology for Sustainable Development (ICICT4SD), Dhaka, Bangladesh, 2021, pp. 115-119, doi: 10.1109/ICICT4SD50815.2021.9396809.
- [21] Vasile, M., Walker, L., Campbell, A. et al. Space object identification and classification from hyperspectral material analysis. Sci Rep 14, 1570 (2024). https://doi.org/10.1038/s41598-024-51659-7
- [22] Tianqi Chen and Carlos Guestrin. Xgboost: A scalable tree boosting system. In Proceedings of the 22nd acm sigkdd international conference on knowledge discovery and data mining, pages 785–794, 2016
- [23] Takuya Akiba, Shotaro Sano, Toshihiko Yanase, Takeru Ohta, and Masanori Koyama. Optuna: A next-generation hyperparameter optimization framework. In Proceedings of the 25th ACM SIGKDD international conference on knowledge discovery & data mining, pages 2623–2631, 2019
- [24] Stellar Science Ltd. Co. (www.stellarscience.com), COAST version 6.31, Albuquerque, NM (2025).